Research Article

Adisu Girma Zewudie, Enyew Amare Zereffa*, Teshome Abdo Segne, H. C. Ananda Murthy, C. R. Ravikumar, Dhanalakshmi Muniswamy, and Bayissa Bekele Binagdie

Biosynthesis of Ag/bentonite, ZnO/bentonite, and Ag/ZnO/bentonite nanocomposites by aqueous leaf extract of *Hagenia abyssinica* for antibacterial activities

https://doi.org/10.1515/rams-2022-0307 received December 13, 2022; accepted February 20, 2023

Abstract: We report the synthesis of Ag/bentonite, ZnO/bentonite and Ag/ZnO/bentonite nanocomposites (NCs) using *Hagenia abyssinica* plant extract and their antibacterial study. The synthesized NCs were characterized by using many advanced techniques. The X-ray diffraction and high resolution transmission electron microscopy analysis confirmed the formation of composites with different phases. The average crystallite size (*D*) values of pure Ag nanoparticles (NPs), ZnO NPs, and activated bentonite (Na-AB) were found to be 8.14, 18.1, and 37.6 nm, respectively. The Ag/bentonite NCs, ZnO/bentonite NCs, and Ag/ZnO/bentonite NCs exhibited the *D* values of 7.4, 9.4, and 9.4 nm, respectively. The Fourier transform infrared spectral analysis revealed the presence of hydroxyl, carbonyl, and

other functional groups on the surface of the synthesized NCs. The transmission electron microscopic analysis revealed the formation of Ag and ZnO NPs with hexagonal, rodshaped, and spherical structures. HRTEM also revealed the presence of (102) plane of ZnO and (220) plane of Ag in Ag/ ZnO/bentonite NCs. The antibacterial activities of the composites suspension were evaluated against Escherichia coli ATCC 25922 and Staphylococcus aureus ATCC 25923 by the disc diffusion and broth dilution methods. The ternary NC and Ag/ZnO/bentonite exhibited better zone of inhibition of 14.3 ± 0.3 and 17.3 ± 0.2 mm at 10 mg·mL^{-1} toward *E. coli* and S. aureus bacterial strains. The minimum inhibitory concentration and minimum bactericidal concentration values of Ag/ZnO/bentonite NCs were found to be 156.25 and 312.5 μ g·mL⁻¹ for *E. coli*. The investigation results revealed that the low temperature bio-synthesized Ag/ZnO/bentonite is a promising bactericide over the binary composites.

Keywords: bentonite, Ag/ZnO/bentonite, *Hagenia abyssinica*, inhibition zone, bactericide

Adisu Girma Zewudie: Department of Chemistry, Madda Walabu University, Robe, Ethiopia

Teshome Abdo Segne: Department of Applied Chemistry, School of Applied Natural Science, Adama Science and Technology University, PO Box 1888, Adama, Ethiopia

H. C. Ananda Murthy: Department of Applied Chemistry, School of Applied Natural Science, Adama Science and Technology University, PO Box 1888, Adama, Ethiopia; Department of Prosthodontics, Saveetha Dental College & Hospital, Saveetha Institute of Medical and Technical Science (SIMATS), Saveetha University, Chennai, 600077, Tamil Nadu, India

C. R. Ravikumar: Research Centre, Department of Science, East-West Institute of Technology, Bengaluru, 560091, India Dhanalakshmi Muniswamy: Department of Physics, Government Science College (Nrupathunga University), Bengaluru, 560 001, India

Bayissa Bekele Binagdie: Adama Public Health Referral and Research Laboratory Center, Adama, Ethiopia

1 Introduction

The pathogenic bacteria that are multidrug resistant are showing up much more frequently nowadays. Antimicrobial resistance has been recognized as an ancient biological phenomenon since the discovery of penicillin [1,2]. European Center for Disease Prevention and Control reported more than hundred thousand healthcare-associated infection cases per day [3,4]. Multidrug-resistant bacteria are a significant public-health threat worldwide, especially in lowand middle-income countries [5]. The resistance of the microbial activity against the classical antimicrobial therapies is highly affecting the human well-being at large [6–8].

Recently, new approaches to tackle bacterial resistance have been investigated employing a variety of inorganic

^{*} Corresponding author: Enyew Amare Zereffa, Department of Applied Chemistry, School of Applied Natural Science, Adama Science and Technology University, PO Box 1888, Adama, Ethiopia, e-mail: enyewama@yahoo.com

2 — Adisu Girma Zewudie *et al.* DE GRUYTER

materials, including metal and metal oxide-based nanoparticles (NPs) and nanocomposites (NCs) [9–13]. The strong antibacterial activities of the biosynthesized Ag NPs on Gram-negative and Gram-positive bacteria, including multidrug-resistant strains were reported by various group of researchers [9-12,14-17]. Zinc oxide (ZnO) is also one of the novel antibacterial materials [18]. By combining ZnO with various band gap semiconductor materials and polymers and controlling the morphology and size of ZnO NPs during the synthesis, researchers are working diligently to improve the antibacterial properties of ZnO [19,20]. A mixture of Ag and ZnO NPs is anticipated to have strong antibacterial activity against a variety of bacteria and efficiency against both Gramnegative and Gram-positive bacteria [21,22]. The clay minerals serve as excellent fillers and support materials for metal and metal oxides to form the composites. The use of Ag or ZnO coated/impregnated clay has been reported to have enhanced the antibacterial activity. The high cation exchange capacity of sodium bentonite clay, obtained mainly through sodium salt activation, has been utilized in the preparation of clay-supported inorganic antibacterial NCs [23]. The synthetic antibacterial clay-supported NCs are prepared by exchanging their native ions with known active species such Ag and ZnO. Clay is widely used due to its great chemical and mechanical stability, specific surface area, and range of surface and structural qualities [23,24]. The antibacterial activity of the extract of H. abyssinica plant against the bacteria was reported by various researchers. According to the reports of these researchers NPs of Ag NPs, Au NPs, and Cu-NPs were successfully synthesized by using the extracts of the medicinal plants such as H. abyssinica, Fagonia indica, and Nerium oleander, respectively [25–27]. The phyto-constituents such as poly-phenols play the roles of reducing and stabilizing agents during the synthesis of the NPs [26]. The synergistic effect of the bioactive compounds from the plant extract and metallic NPs has been proved to be beneficial against pathogens. Many researchers have tried to support metal and metal oxides over the clay materials to get composites which work as antibacterial agents, but no work has been reported on the biosynthesis of Ag/bentonite, ZnO/bentonite, and Ag/ZnO/bentonite NCs. Hence, the aim of this research work was to synthesize the novel NCs by using the calcium-rich and sodium carbonate (Na₂CO₃)-activated local bentonite and leaf extract of *H. abyssinica* medicinal plant at low temperature. All the synthesized NCs, Ag/bentonite, ZnO/bentonite, and Ag/ZnO/bentonite were characterized and their antibacterial activities were investigated.

2 Methods and materials

2.1 Materials and chemicals

The analytical grade chemicals: AgNO₃ (99.98%), Zn (CH₃COO)₂·2H₂O (99.9%), and NaOH were used without any further purification. Bentonite was collected from the site at Mille, Afar Region, North Eastern Ethiopia. The leaves of *Hagenia abyssinica* plant were collected from Adele town, Oromia regional state, South Eastern Ethiopia. The bacterial strains, Gram-negative (*Escherichia coli* ATCC 25922) and Gram-positive (*Staphylococcus aureus* ATCC 25923) were collected from the Adama Public Health Research and Referral Laboratory Center for the antibacterial activity studies.

2.2 Experimental procedure

2.2.1 Purification of bentonite

The collected natural bentonite was sun dried, crushed, milled, and later screened using a 250 μ m sieve. To remove quartz, carbonates, calcites, and iron hydroxide, the sieved bentonite was dispersed in distilled water (100 g·1 L⁻¹) at room temperature and clay fraction was recovered with a homogenizer (1,000 rpm) for 1 h. This process was repeated four times, in order to obtain the samples in a pure form. The suspensions were allowed to stand for 24 h to settle the impurities. The supernatant was decanted and the precipitate was discarded. The suspension was centrifuged at 3,000 rpm for 20 min, and then dried in an oven at 60°C, grounded, and sieved using a 63 μ m size sieve, and stored in the closed plastic bottles for further characterization and studies [28].

2.2.2 Activation of bentonite clay by Na₂CO₃

Activation of the purified raw bentonite rich with calcium was carried out using the method discussed in the past work [29] by slight modification. Purified bentonite (PB) powder of 100 g was dispersed in 1 L distilled water to form a suspension. Then, 5 g of Na₂CO₃·10H₂O was added to the suspension, stirred, and boiled for 1 h to get a stable aqueous dispersion. The suspension was allowed to cool to room temperature and diluted with 1 L of distilled water, and allowed to stand for 24 h. The supernatant was decanted and the precipitate was discarded.

The bentonite suspension was centrifuged at 3,000 rpm for 20 min, then dried in an oven at 60°C for 12 h and ground to obtain an activated bentonite powder.

2.2.3 Preparation of aqueous plant leaf extract

About 25 g of the powdered leaves of *H. abvssinica* plant was taken in a 1,000 mL conical flask containing 400 mL of deionized water. The flask was then covered with aluminum foil to prevent the effect of light. After that, the contents of the flask were mixed well using a magnetic stirrer for 90 min and allowed to warm at 50°C for 1 h. Later the solution was allowed to cool down to room temperature overnight. The prepared solution was filtered through Whatman No. 1 filter paper to obtain a clear solution. The filtrate was stored at 4°C [25]. The phytochemical screening was conducted to identify the biomolecules present in the leaf extract of H. abyssinica plant using the standard testing methods [30].

2.2.4 Synthesis of Ag NPs

Plant leaf extract of 100 mL was mixed with 100 mL of 0.2 M AgNO₃ solution (1:1) by maintaining the temperature at about 50°C for 2h. The color change was checked periodically after 30 min of duration. Then, the mixture was incubated at room temperature for 24 h and the solution was centrifuged for 15 min at 3,000 rpm. The obtained Ag NPs was washed with deionized water and ethanol to remove any impurities. Then, the NPs were allowed to dry, and ground so as to be used for further analysis [25].

2.2.5 Synthesis of ZnO NPs

Leaf extract of 100 mL was added dropwise to 100 mL of 0.2 M zinc acetate solution and the mixture was vigorously stirred at 80°C for 30 min. The solution was continuously stirred for 3 h at 80°C by adjusting the pH of the solution to 12 using 1 M NaOH solution. Then, the solution was cooled and centrifuged at 3,000 rpm for 20 min to separate the precipitate. The precipitate was washed several times with double distilled water and dried at room temperature. The solid powder was ground using an agate mortar and placed in a furnace at 450°C for 3 h for calcination [31].

2.2.6 Synthesis of Ag/bentonite NCs

The activated bentonite was dispersed in 100 mL of distilled water and stirred for 30 min. Then 100 mL of 0.2 M

silver nitrate solution was added to it. Next, 100 mL of leaf extract was also added to the solution slowly dropwise with constant stirring at about 50°C. The dark brown-colored mixture was made to settle down overnight. The settled NC was collected, washed with distilled water and ethanol four times to remove the bioresidues. Furthermore, the washed material was dried in a hot-air oven at 80°C for 12 h to obtain Ag-clay powder [32,33].

2.2.7 Synthesis of ZnO/bentonite NC

The activated bentonite was dispersed in 100 mL of distilled water and stirred for 30 min. Then 100 mL of 0.2 M zinc acetate was added to the bentonite suspension and vigorously stirred. Next, 100 mL aqueous extract of H. abyssinica was added dropwise with constant stirring for 30 min at room temperature. The color change was observed from white to light brown. The solution was continuously stirred for 3 h at 80°C by adjusting the pH of the solution to 12 using 1 M of NaOH solution. The obtained light brown suspension was centrifuged at 3,000 rpm for 20 min. The precipitate formed at the bottom of the container was washed with double distilled water and ethanol. Then, the samples were dried at room temperature, calcined at 550°C for 1 h, and stored in a glass bottle [34].

2.2.8 Synthesis of Ag/ZnO/bentonite NC

A 2.2 g of ZnO/bentonite was dispersed in 100 mL distilled water for 30 min at room temperature. Then, a mixture of 100 mL of 0.2 M of a silver nitrate solution and 100 mL of plant leaf extract was mixed with this solution slowly with constant stirring at 50°C. The mixture was kept overnight, centrifuged at 3,000 rpm for 20 min, and washed with the double distilled water followed by ethanol four times to remove the bioresidues. Furthermore, the washed material was dried in oven at 80°C and ground to get the powder [35,36].

2.3 Characterization

The X-ray diffraction (XRD) analysis was used to study the crystalline structures of PB, sodium-activated bentonite (Na-AB), synthesized NPs, and NCs using an X-ray diffractometer (XRD700, Shimadzu Co., Japan). The diffraction patterns were recorded within a range of 2θ from 10° to 80° for Ag and ZnO NPs and from 5° to 80° for PB, Na-AB, and NCs. The diffraction data were recorded at 40 kV and current of 30 mA in a continuous scan mode with scan rate of 3°·min⁻¹ by using CuKα radiation with a wavelength of 1.5406 Å [24]. The average crystallite sizes (D)of the powders were calculated by using Debye-Scherrer's formula. The diffused reflectance spectra were recorded in the wavelength range of 200-800 nm using a UV spectrophotometer (UV3600plus, Shimadzu, Japan). Fourier transform infrared (FT-IR; PerkinElmer) spectroscopy helps to ascertain the identity of various phyto-constituents involved in the reduction and stabilization of the NPs and NCs [37]. The scanning electron microscopy with energy-dispersive X-ray spectroscopy (SEM-EDX; EVO18 model with low vacuum facility and ALTO1000Cryo attachment) and transmission electron microscope with high-resolution (HRTEM; JEOL JEM2100) were used for understanding the morphological and structural features of Ag and ZnO NPs. The selected area electron diffraction (SAED) was performed to confirm the crystal structure of NPs and NCs. The particle size and SAED patterns were computed by using image J and Microsoft paint software.

2.4 Antibacterial test

The antibacterial activities of *H. abyssinica* leaf extract, PB, Na bentonite, Ag NPs, ZnO NPs, Ag/bentonite, ZnO/bentonite, and Ag/ZnO/bentonite NCs were investigated against Gram-negative bacteria *E. coli* ATCC 25922 and Gram-positive bacteria *S. aureus* ATCC 25923 through disc diffusion and broth dilution method in Adama Public Health Research and Referral Laboratory Center.

2.4.1 Disc diffusion methods

Muller-Hinton Agar and Sheep Blood Agar Media were prepared by dissolving 38 g of Muller-Hinton powder and 50 mL of Sheep Blood in 1L of distilled water separately and then sterilized by autoclave at 121°C and 15 pound pressure for 20 min. After cooling, 20 mL of medium was added aseptically to sterilized Petri dishes. Then the Petri dishes were labeled and incubated until they solidify. The pH of the medium is generally maintained around the physiological pH of 7.4. The bacterial cultures were maintained on blood agar at 37°C. The bacterial suspension was prepared by taking it from blood agar and dissolving in sterile normal saline until the concentration of bacterial suspensions were achieved to 1×10^7 colony forming units (CFU)·mL⁻¹ by comparison with the 0.5 McFarland Standard. Then 100 µL of standardized culture of test bacteria was evenly spread onto the surface of the Muller-Hinton agar

plates using the sterile cotton swabs. The antibiotic Cotrimoxazole was used as the positive control to study the efficiency of the as-synthesized NCs and dimethyl sulfoxide (DMSO) solvent was used as the negative control. To test each targeted material, 20 mg of as-prepared sample was dissolved in 1 mL DMSO (20 mg·mL⁻¹). From 20 mg·mL⁻¹ concentration of each sample, 10, 5, and 2.5 mg·mL⁻¹ were diluted serially for PB, Na-AB, ZnO NPs, and ZnO/bentonite NCS and 5, 2.5, and 1.25 mg·mL⁻¹ were serially diluted from 10 mg mL⁻¹ for Ag NPs, Ag/bentonite, and Ag/ZnO/bentonite NCs and 6 mm diameter disc was saturated with 20 uL from each concentration and 25 ug of Contrimoxazole (positive control) and placed on a plate covered with lids and incubated at 37°C and 0% CO2 for 24 h [38]. The diameters of the inhibition zone were measured. All the antibacterial tests were carried out in triplicate and the averages were reported [39].

2.4.2 Broth dilution methods

Determination of the minimum inhibitory concentration (MIC) and minimum bactericidal concentration (MBC): Ag/ZnO/bentonite NCs suspension was tested for the bactericidal effect using both the microbial cultures selected for the study. The lowest concentration of the material that inhibits the growth of an organism was defined as the MIC [40]. The serial dilution method was employed to determine the MIC of the Ag/ZnO/bentonite NC. Each of the ten test tubes was filled with 2 mL of the liquid Muller-Hinton Agar medium. In the test tube number 1, 2 mL solution containing 20 mg·mL⁻¹ of NC that had been sonicated at room temperature was added and mixed thoroughly with the culture medium. The concentration of NCs in test tube 1 becomes 10 mg·mL⁻¹. Then, 2 mL of the content of test tube number 1 was added to test tube number 2 and mixed completely. This process was performed serially to test tube number 11. Consequently, 2 mL content of test tube number 11 was discarded. Finally, 0.2 mL of standard microbial suspensions of E. coli and S. aureus containing $1 \times 10^8 \, \text{CFU} \cdot \text{mL}^{-1}$ microorganisms were added to the test tubes from 1 to 10, and the test tubes were incubated at 35°C for 24 h. Then, the microbial growth was studied by turbidity observation. The experiments also included both the positive control and negative control. All the experiments were carried out in triplicate. The MBC of NPs was determined from the batch culture studies. For growth inhibitory concentration (MIC) the presence of viable microorganisms was tested and the lowest concentration causing bactericidal effect was reported [41].

3 Results and discussion

3.1 Characterization

3.1.1 UV-visible diffuse reflectance spectra and band gap analysis

The Kubelka–Munk plots of the synthesized samples are given in Figure 1(a–e). The synthesized Ag and ZnO NPs showed the absorbance maxima at 313 and 311 nm, respectively.

The synthesized NCs Ag/bentonite, and ZnO/bentonite showed the absorbance maxima at 313.7 and 316 nm, respectively. The Ag/ZnO/bentonite NC showed two maximum absorption peaks at 318 and 372.7 nm due to the existence of both Ag and ZnO NPs in the composite. This result is in agreement with a previous study that claimed ZnO NPs had an absorbance peak between 310 and 360 nm [42]. The observed peak shift in composites was in compliance with result of the published work [23,43]. The direct band gap energy $E_{\rm g}$ values of Ag NPs, ZnO NPs, Ag/bentonite NCs,

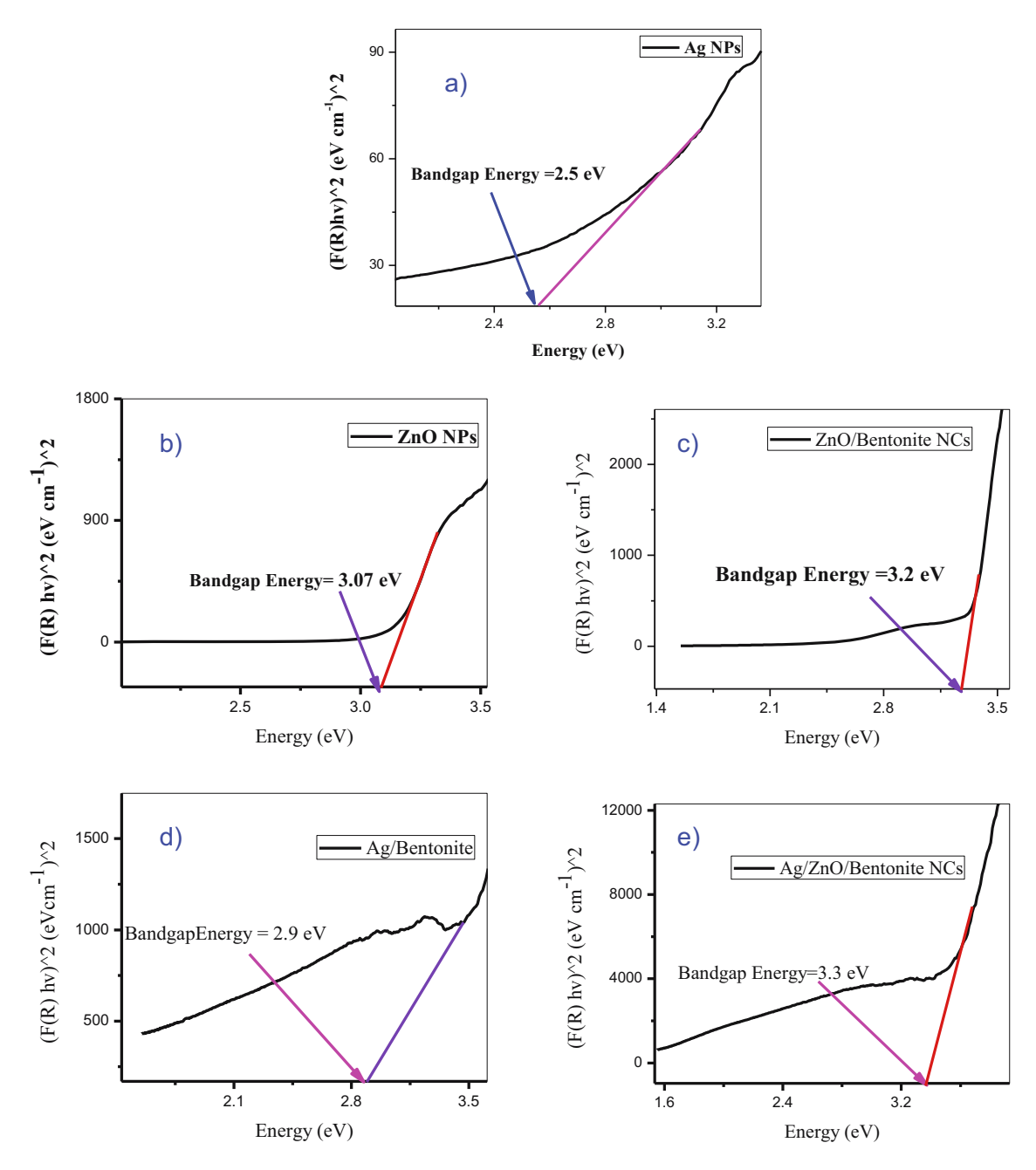


Figure 1: Bandgap energy values of synthesized nanoparticles and nanocomposites. (a) Ag NPs, (b) ZnO NPs, (c) Ag/Bentonite NCs, (d) ZnO/Bentonite NCs and (e) Ag/ZnO/Bentonite NCs.

ZnO/bentonite NCs, and Ag/ZnO/bentonite NCs were found to be 2.5, 3.07, 2.9, 3.2, and 3.3 eV, respectively, as depicted in Figure 1.

3.1.2 XRD pattern analysis

The XRD patterns of the PB and Na-AB samples are depicted in Figure 2. It shows the basal reflections at the 2θ positions, 6.24 (for PB), 6.9 (for Na-AB), 15.6 (for PB), 15.9 (for Na-AB), 19.8, 26.4, 29.4, 34.5, 61.4°, *etc.* According to the crystal data file (JCPDS 02-0037), these basal reflections correspond to $d_{(001)}$, $d_{(003)}$, $d_{(100)}$, $d_{(400)}$, $d_{(330)}$, $d_{(105)}$, and $d_{(300)}$, respectively. This result is in agreement with the results of the past work [44].

The $d_{(001)}$, $d_{(100)}$, $d_{(104)}$, and $d_{(061)}$ diffractions of the main montmorillonite component of PB and Na-AB are seen at 6.24 (for PB), 6.9 (for Na-AB), 15.6 (for PB), 15.9 (for Na-AB), 19.8, 34.5, and 61.4° with the distances of ~14 for PB, 12.8 for Na-AB, 5.67 for PB, 5.56 for Na-AB, 4.48, 2.59, and 1.51 Å, respectively (Figure 2). The peaks originating from the non-clay components (dolomite [D] and quartz [Q]) are observed at 26.4° and 29.4° with the $d_{(400)}$ and $d_{(330)}$ values of 3.37 and 3.04 Å, respectively. It may be concluded from the comparison of the intensities of $d_{(001)}$ peak of PB and Na-AB that the diffractions of the non-clay minerals, the main component of bentonite, montmorillonite, and the fractions of quartz and dolomite are in small quantities [45].

The XRD pattern of the PB powder shows that the bentonite used for this work is smectite with reflection (001) located at 14 Å. This supported that the local bentonite clay

used is calcium-rich bentonite [46]. The larger $d_{(001)}$ distance of PB (~14 Å) than that of Na-montmorillonite (12.8 Å) makes it clear that the used bentonite was calcium-rich bentonite [45]. The Na-montmorillonite obtained by soda activation has a lower $d_{(001)}$ spacing (~12.8 Ű) than that of the Ca-montmorillonite (14 Ű) (Table 3), suggesting that the Na⁺ ions replaced Ca²⁺ ions in the montmorillonite interlayer. This finding is in agreement with the result of the previously published work [47].

The diffraction pattern of the Ag NPs shows sharp peaks at $2\theta = 38.20^{\circ}$ (111), 43.21° (200), 64.56° (220), and 77.48° (311) confirming their crystallinity (Figure 3). The diffraction results were in good agreement with the data of JCPD file No. 00-004-7383 (Fm3m). A similar finding was reported earlier [48]. The average crystallite size of Ag NPs was found to be 8.14 as deduced using the Debye–Scherrer equation (1) [49]. This small crystallites size is the results of using excess leaf extract (1:1) ratio and it confirms the better capacity of the phytochemicals toward the reduction and stabilization of NPs.

$$D = K\lambda/\beta \text{Cos}\theta, \tag{1}$$

where λ is the X-ray wavelength coming from Cu-K α (1.540560 Å), β is the full width at half maxima of the diffraction peak in radians, θ is the Braggs angle in degrees, and K is the shape factor and its value is equal to 0.9.

The XRD pattern of the synthesized ZnO NPs also clearly indicates the formation of wurtzite structure for ZnO (Figure 4). The sharp diffraction peaks were observed at 2θ values 31.9°, 34.5°, 36.3°, 47.6°, 56.6°, 62.9°, 66.5°, 68°, and 69.1° The peaks were indexed to (100), (002),

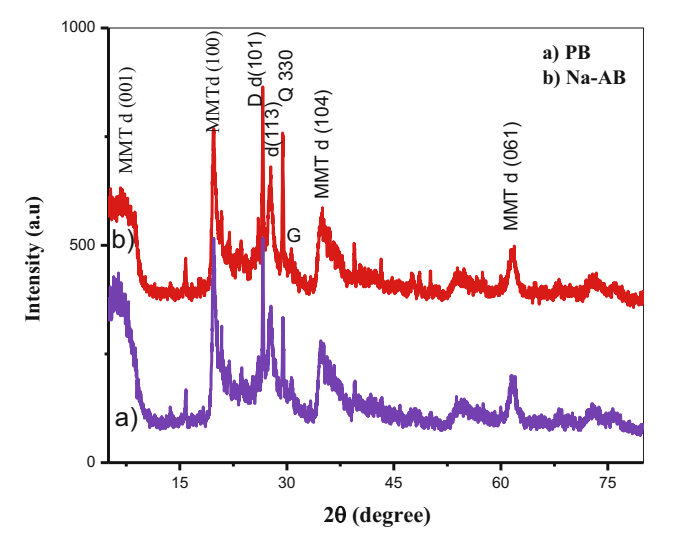


Figure 2: XRD patterns of (a) PB and (b) Na-AB.

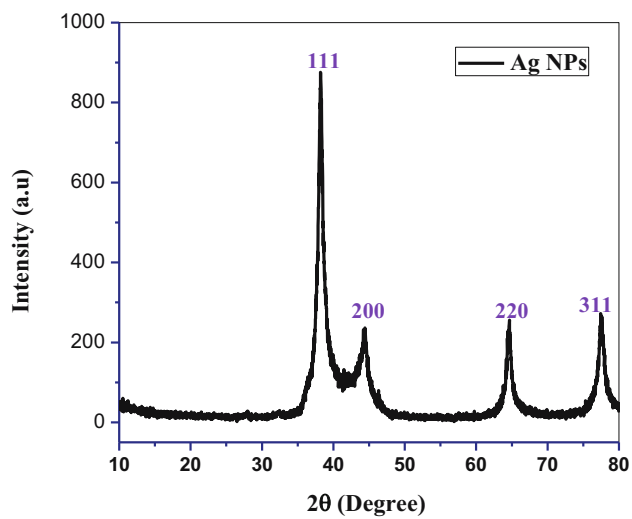


Figure 3: XRD patterns of synthesized Ag NPs.

(101), (102), (110), (103), (200), (112), and (201) diffraction planes, respectively. All the indexed peaks matched with the hexagonal phase in accordance with the data from the JCPDS card No. 36-1451. It is also in good agreement with the previous findings [50]. The FWHM results revealed the fringe widths for the planes, $d_{(100)} = 2.806$ Å, $d_{(002)} = 2.60$ Å, and $d_{(101)} = 2.487$ Å. This is in compliance with the results presented in the earlier work [50,51]. The average crystallite size of ZnO NPs was calculated from three strong peaks (31.8°, 34.5°, and 36.3°) and estimated to be 18.1 nm.

From the XRD patterns presented in Figure 5, the characteristic peaks of the bentonite are shown at 2θ values of 6.9°, 19.8°, and 27.7°. The prominent peaks of ZnO were observed at 2θ of 31.7°, 34.3°, 36.3°, 47.5°, 56.7°, 62.9°, and 68.01 which can be attributed to (100), (002), (101), (102), (110), (103), (112), and (201) planes, respectively. In case of ZnO/bentonite NCs, the reduction in the peak intensities was observed [52]. In the XRD pattern of ZnO-bentonite NCs (Figure 5(a)), the left side peaks (below 2θ of 30°) strongly exhibited the bentonite character and right side peaks (2θ of 30°) exhibited the ZnO character. The intensity of the characteristic peaks of the bentonite is lower than that of activated bentonite, which is possibly due to the intercalation of ZnO into the interlayers of bentonite, which changed the structure of host materials.

The XRD patterns of Ag/bentonite and Ag/ZnO/bentonite NCs are presented in Figure 5(b) and (c). The peaks are shown at 2θ values of 6.9°, 19.8°, and 27.7° and at 6.9°, 19.6°, and 26.6° for Ag/bentonite and Ag/ZnO/bentonite, respectively. The obtained patterns are in compliance with the other reported works [53]. After the intercalation of Ag and ZnO into the clay, additional peaks were observed

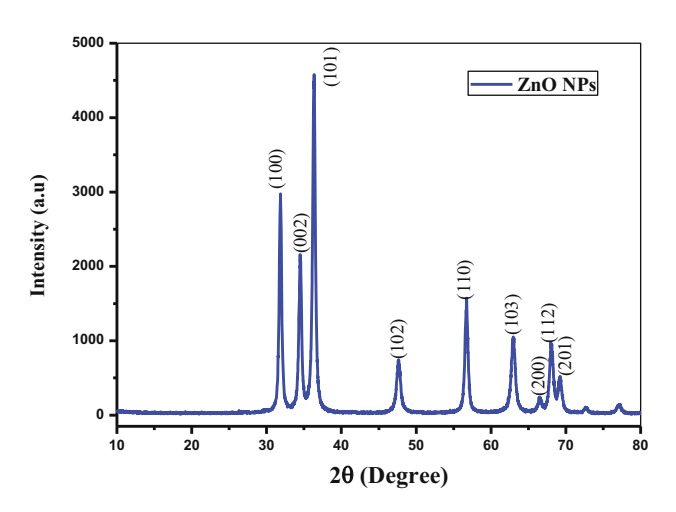


Figure 4: XRD patterns of synthesized ZnO NPs.

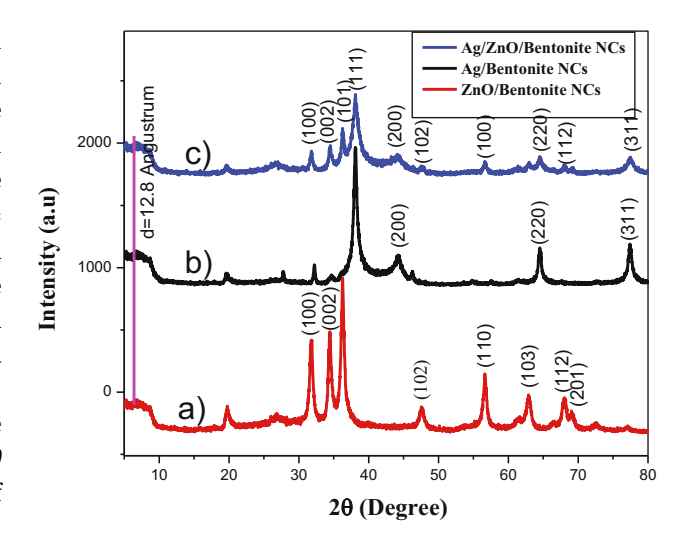


Figure 5: XRD patters of ZnO/Bentonite NCs (a), Ag/Bentonite NCs (b), and Ag/ZnO/Bentonite NCs (c).

corresponding to the formation Ag and ZnO in the composites. These peaks were reflected at $2\theta = 38^{\circ}$ for Ag which can be attributed to the (111) plane of the face-centred cubic silver crystals [54]. The appearance of the peaks at $2\theta = 32^{\circ}$, 34°, and 36° corresponding to (100), (002), and (101), reflects the presence of wurtzite phase of ZnO [55]. The presence of the diffraction patterns of Ag, ZnO, and bentonite confirms that the prepared composites are composed of these three species.

XRD patterns have also been used to calculate the average crystalline sizes (D) of samples with the help of Scherrer equation (equation (1)). The calculated *D* values of Ag NPs, ZnO NPs, and Na-AB were found to be 8.14, 18.1, and 37.6 nm, respectively. The D values of Ag and Na-AB in Ag/bentonite NCs were found to be 12 and 15.8 nm and the D values of ZnO and Na-AB in ZnO/bentonite NCs were found to be 13 and 11.7 nm. However, the D values of Ag, ZnO, and Na-AB in Ag/ZnO/bentonite NCs were estimated to be 7.4, 9.4, and 9.4, respectively. The D values in NCs were observed to have decreased due to intercalation of NPs into Na-bentonites. Hence, the intercalation process causes structural changes in Na-bentonite samples. It may be due to the presence of the strong electrostatics attraction and hydrogen bonding forces in between Na-bentonite and intercalate NPs [56].

3.1.3 FT-IR analysis

Figure 6 depicts the FT-IR spectrum of the plant extract with the peak observed at 3,400 cm⁻¹ typical of –OH (alcohol) group. The peaks appeared at 2,930 and 2,845 cm⁻¹ correspond

to C–H (stretch) for alkanes. The peaks at 1,628 and 1,010 cm⁻¹ correspond to conjugated alkenes and C–O stretch of alcohol. The peak observed between 1,000 and 1,500 cm⁻¹ is due to the presence of the C–O bond. The presence of secondary amine was also detected at 1,628 cm⁻¹ [57].

Figure 7 shows the FT-IR spectrum of Ag NPs. The peaks appeared at 3,420, 2,902, 1,600, and 1,304 cm⁻¹ correspond to –OH stretching, C–H bending, C=O stretching, C=C stretching vibrations, respectively. The peaks at 1,170 and 1,014 cm⁻¹ are assigned to the absorption of C–O and C–O–C bonds, respectively. In addition to this, the spectrum of Ag NPs shows peaks corresponding to the band at 750 cm⁻¹ which may be due to the interaction of Ag with protein molecules of extract. These results demonstrate that many organic constituents of plant extract were adsorbed onto the surface of the Ag NPs.

Figure 8 shows the FT–IR spectrum of ZnO NPs (calcined at 450°C for 3 h). The bands were observed at 3,405, 2,350, 2,169, 1,989, 1,439, 1,000, 881, and 526 cm⁻¹. The broad peak around 3,405 cm⁻¹ corresponds to H-bonded or OH stretch bond vibration of polyphenols and flavonoids. The peak at 2,350 cm⁻¹ corresponds to N–H stretching or the C=O stretching vibrations [58]. The band which appeared at 2,169 cm⁻¹ is due to C=C stretching [59]. C=C=C stretching was observed at 1,989 cm⁻¹. The band at 1,439 cm⁻¹ was attributed to the C–C stretching of the aromatic ring [60]. The band at 1,000 cm⁻¹ is assigned to C–O stretching. The peak appeared in the region between 400 and 600 cm⁻¹ is allotted to Zn–O [61]. So, the band located near 600 cm⁻¹ is assigned to Zn–O stretching vibration [62].

The FT-IR spectra of Ag/bentonite, ZnO/bentonite, and Ag/ZnO/bentonite NCs are displayed in Figure 9(a)-(c). In

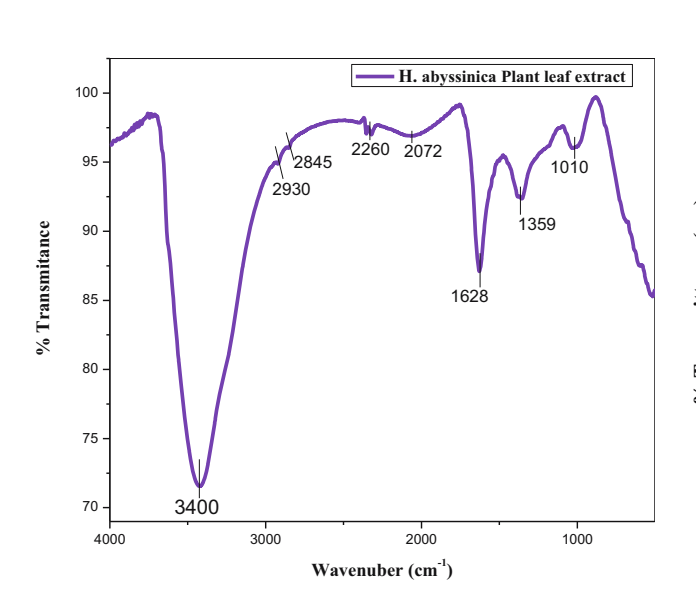


Figure 6: FT-IR spectra of *H. abyssinica* plant leaf extract.

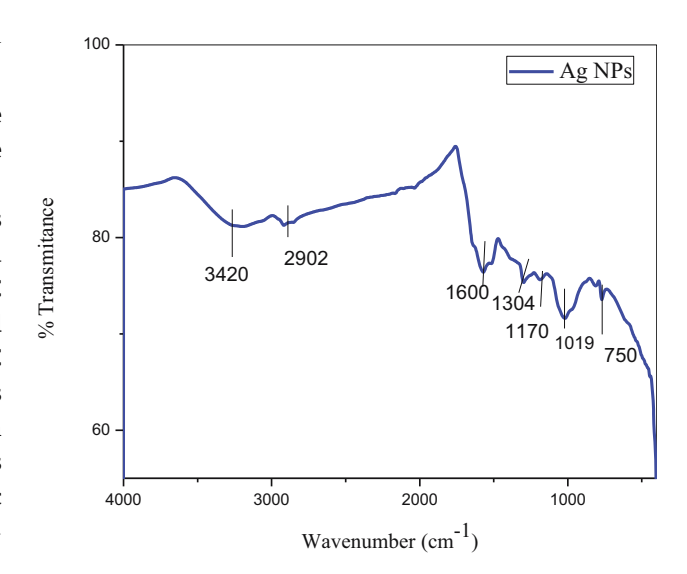


Figure 7: FT-IR spectra of synthesized Ag NPs.

addition to the appearance of similar peaks discussed earlier, a peak appeared at 1,000 cm⁻¹ is attributed to the stretching vibration of Al–O and Si–O. The Al–O–Si deformation and Zn–O stretching vibrations are shown in the range of 420–520 and 476 cm⁻¹ due to Zn–O stretching vibration [34,52]. This result revealed the involvement of the plant extract in the formation of NCs and certain interaction between the clay and the NPs.

3.1.4 SEM-EDX of ZnO NPs

The SEM image is shown in Figure 10, with the hexagonal, rod-shaped, and irregularly shaped morphology

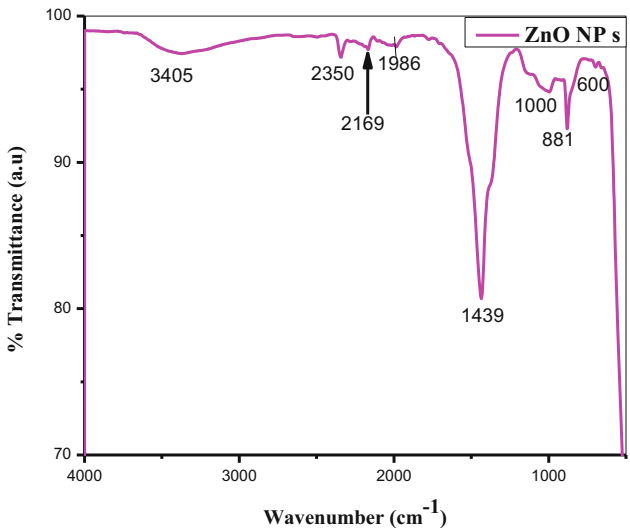


Figure 8: FT-IR spectra of synthesized ZnO NPs.

for ZnO NPs. The EDX analysis of the calcined sample indicates the presence of elemental Zn and O.

Figure 10(b) reveals the SEM micrographs of ZnO/bentonite and Ag/bentonite NCs. The SEM micrographs of these two binary system composites are almost uniform in morphologies. The SEM image of ternary system (Ag/ZnO/bentonite) is similar to that of binary system, but the number of particles impregnated/loaded per unit area is more in the ternary system. The EDX analysis of Ag/bentonite, ZnO/bentonite, and Ag/ZnO/bentonite confirmed the presence of the major elements Ag, Zn, Si, Al, and O in the binary and ternary systems.

3.1.5 Transmission electron microscopic (TEM) images and SAED

The TEM images (Figure 11) revealed the hexagonal, rod-shaped, and spherical morphologies for ZnO/bentonite NC with the average size ranging between 5 and 35 nm (histogram 11b). The average diameter of ZnO/bentonite was found to be around 18.5 nm.

The TEM micrographs of Ag/bentonite NC with spherical, cylindrical, as well as hexagonal shapes are presented in Figure 11(e). These particles were found to vary in size from 3 to 20 nm with an average particle size of 10.8 nm, as determined by image J Software and depicted in Figure 11(f).

HRTEM of the composite contains crystal planes of different constituents of the composites. A lattice spacing of 0.19 nm, corresponding to the planes of (102) confirms

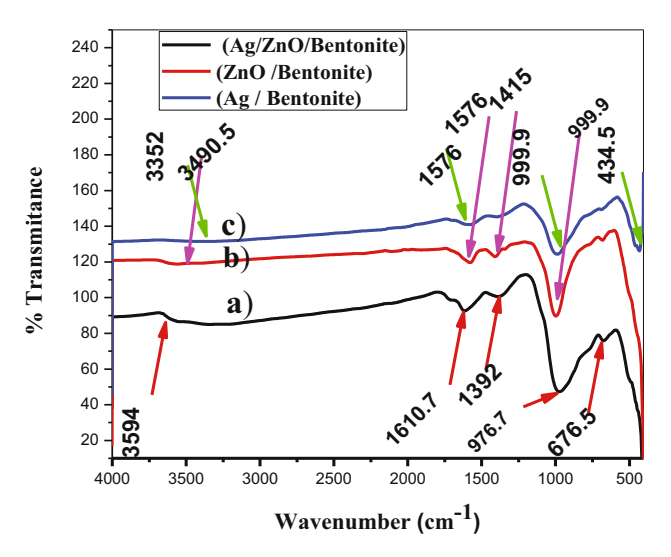


Figure 9: FT-IR spectra of synthesized Ag/Bentonite (c), ZnO/Bentonite (b) and Ag/ZnO/Bentonite (a) nanocomposites using *H. abyssinica* plant leaf extract.

the wurtzite structure for ZnO (Figure 12(a)). Figure 12(b) shows the SAED pattern and the results are consistent with the XRD diffractogram obtained for ZnO NPs, which contained eight concentric rings (small spots making up a ring) each corresponding to specific set of crystal planes. The *d*-spacing values for all the spots depicted in the SAED pattern matched with XRD patterns of ZnO NPs. The HRTEM images as shown in Figure 13(e) and (f), revealed the *d*-spacing values of 0.19 and 0.153 nm, which are consistent with the (102) plane of ZnO and (220) plane of Ag NPs (Table 1).

3.2 Antibacterial activity analysis

3.2.1 Disc diffusion methods

The corresponding sample denoted by X_n is as illustrated in Tables 2 and 3. The standard Contrimoxazole (Ct) of 25 µg exhibited the antibacterial activities within the range of 18.3 \pm 0.3 to 23.7 \pm 0.3 and 20.7 \pm 0.3 to 24.3 \pm 0.3 for E. coli and S. aureus, respectively. DMSO (DM) exhibited no activity (6 mm) on both bacterial strains and it was used as solvent in samples serial dilution. The antibacterial test results of the synthesized samples and the details are summarized in Tables 2 and 3. The presence of an inhibition zone indicates the antibacterial effect of the NPs and NCs. The results revealed that the PB (denoted with "X₆") and Na-bentonite (denoted with "X₇") do not exhibit any antibacterial effect. While the plant extract (denoted with "X₈") exhibited an inhibition zone and the results were more pronounced on Grampositive bacteria (S. aureus). The plant extract showed significant antibacterial activities (P < 0.05) against both tested bacterial strains. The maximum inhibition zone of plant extract toward S. aureus was 10 ± 0.0 mm at 20 mg·mL^{-1} and minimum was 8.3 ± 0.3 mm at 2.5 mg·mL⁻¹. While, the maximum and minimum values were found to be 9.1 ± 0.3 mm at $20 \text{ mg} \cdot \text{mL}^{-1}$ and $7.3 \pm 0.3 \text{ mm}$ at $2.5 \text{ mg} \cdot \text{mL}^{-1}$, respectively, toward *E. coli* (detail in Table 3).

The antibacterial effect of the plant extract is due to the large number of different chemical compounds. Tannins and flavonoids are the simple phenolic compounds that serve as defense against pathogens and herbivores. The antioxidant property of phenolic compounds is attributed to the free radical scavenging capacity, donating hydrogen atom, electrons, or chelated metal cations [63]. Thus chemical components can affect multiple target sites against the bacterial cells [64]. *E. coli* bacteria are more resistant against *H. abyssinica* plant

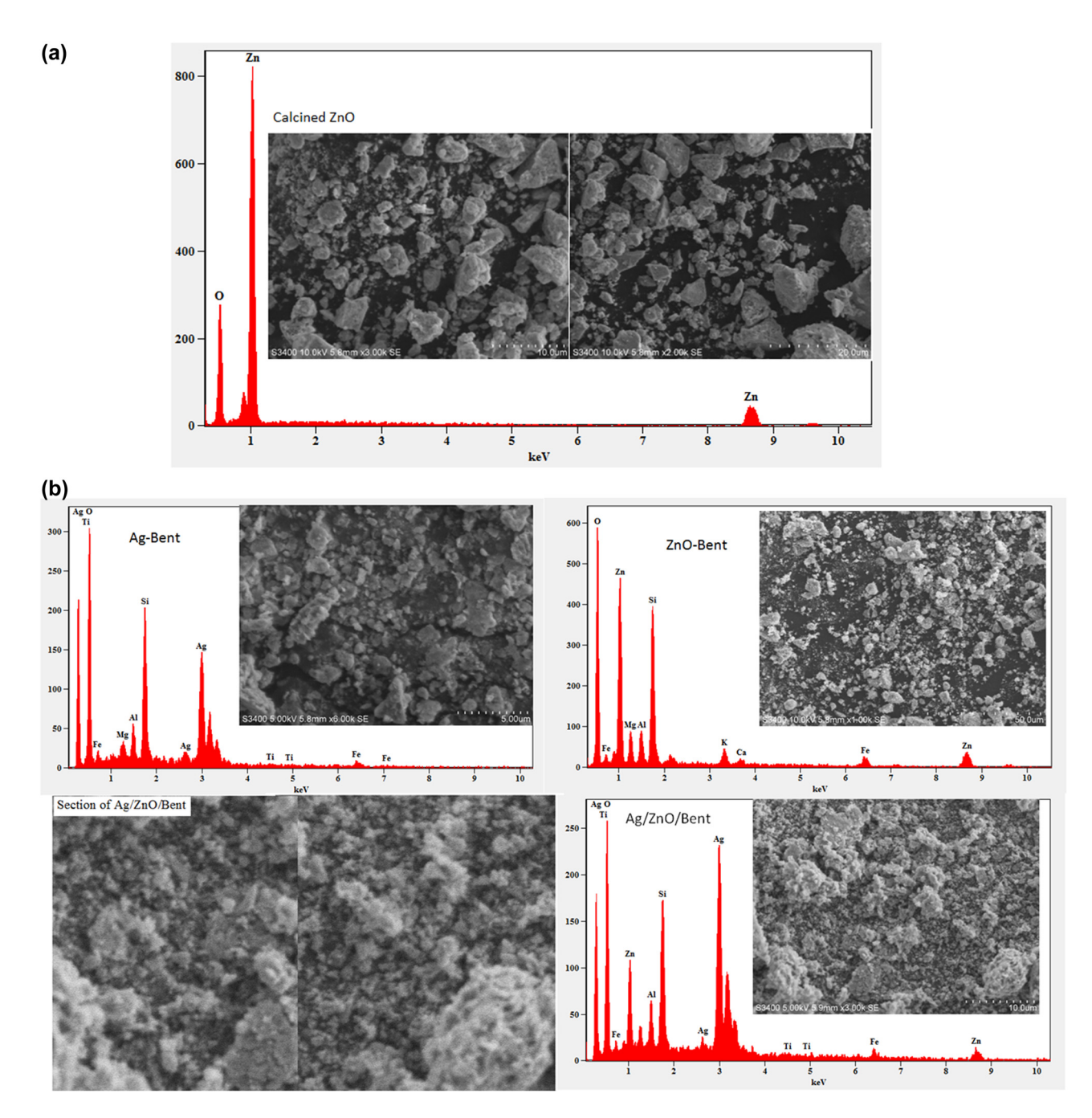


Figure 10: (a) SEM-EDS spectrum of ZnO NPs, (b) SEM micrographs and EDX of Ag/bentonite, ZnO/bentonite, and Ag/ZnO/bentonite NCs.

leaf extract than *S. aureus*. This additional membrane means that there is also an extra membrane layer termed periplasm, which develop more resistance than Grampositive that contain a thick layer of peptidoglycan in their cell walls [65].

The antibacterial activity of the biosynthesized Ag NPs was investigated against $E.\ coli$ and $S.\ aureus$. The viable disc diffusion method was performed to assess the antibacterial properties of Ag NPs at various concentrations (10, 5, 2.5, and 1.25 mg·mL $^{-1}$) (denoted with "X₁").

The growth results of *E. coli* and *S. aureus* ATCC that were exposed to various concentrations of Ag NPs are indicated in Table 2. The results show that Ag NPs exhibited significant antibacterial activities against both bacteria even for the lowest concentration $(1.25 \text{ mg} \cdot \text{mL}^{-1})$.

The Ag NPs (denoted with "X1") showed the inhibition zones between 10.3 \pm 0.3–11.6 \pm 0.3 and 11.3 \pm 0.3–14.3 \pm 0.3 mm for *E. coli* and *S. aureus* at 1.25–10 mg·mL⁻¹, respectively (Table 2). It can be concluded that *S. aureus* bacteria was more sensitive toward Ag NPs. This is due to bacterial

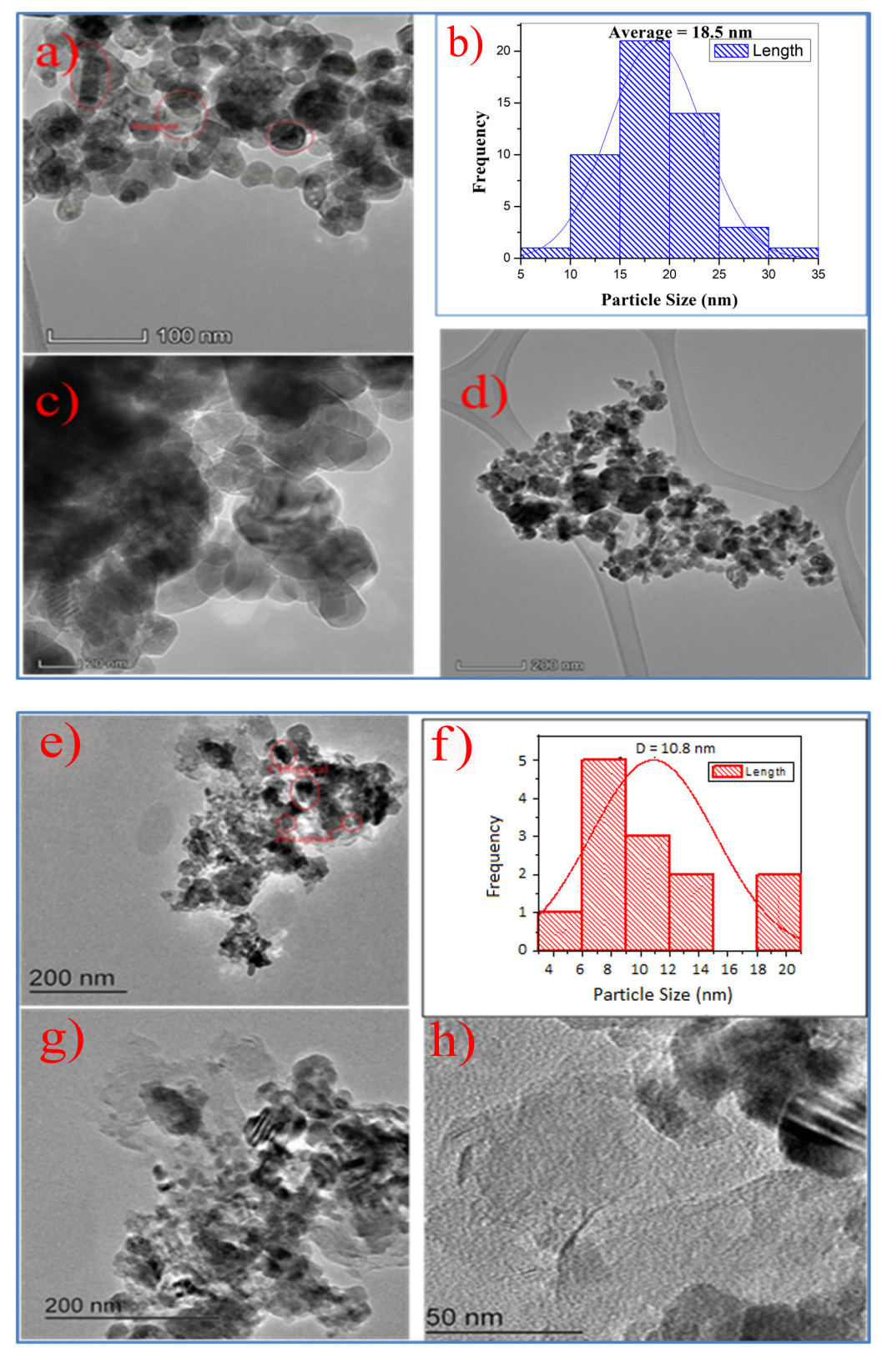


Figure 11: TEM images of ZnO/bentonite NC (a, c, and d) and Ag/bentonite NC (e, g, and h) at different scales, and histogram shows size distribution of ZnO/bentonite NC (b) and Ag/bentonite NC (f) obtained from TEM image.

12 — Adisu Girma Zewudie *et al.* DE GRUYTER

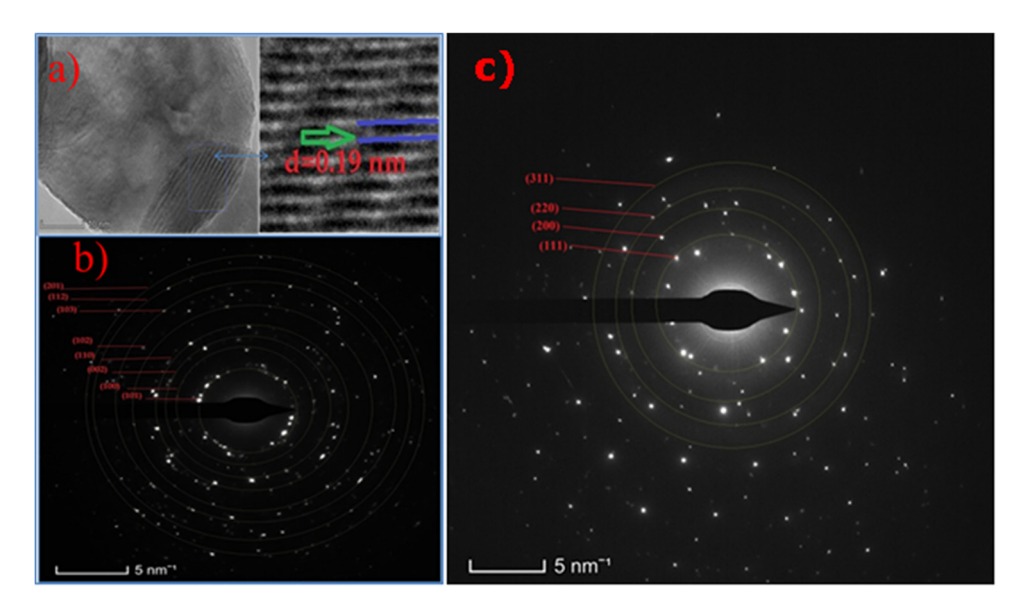


Figure 12: HRTEM of Ag/ZnO/bentonite NC (a), SAED pattern of ZnO NPs (1-8 spots) (b), and Ag NPs (1-4 spots) (c) with crystal planes.

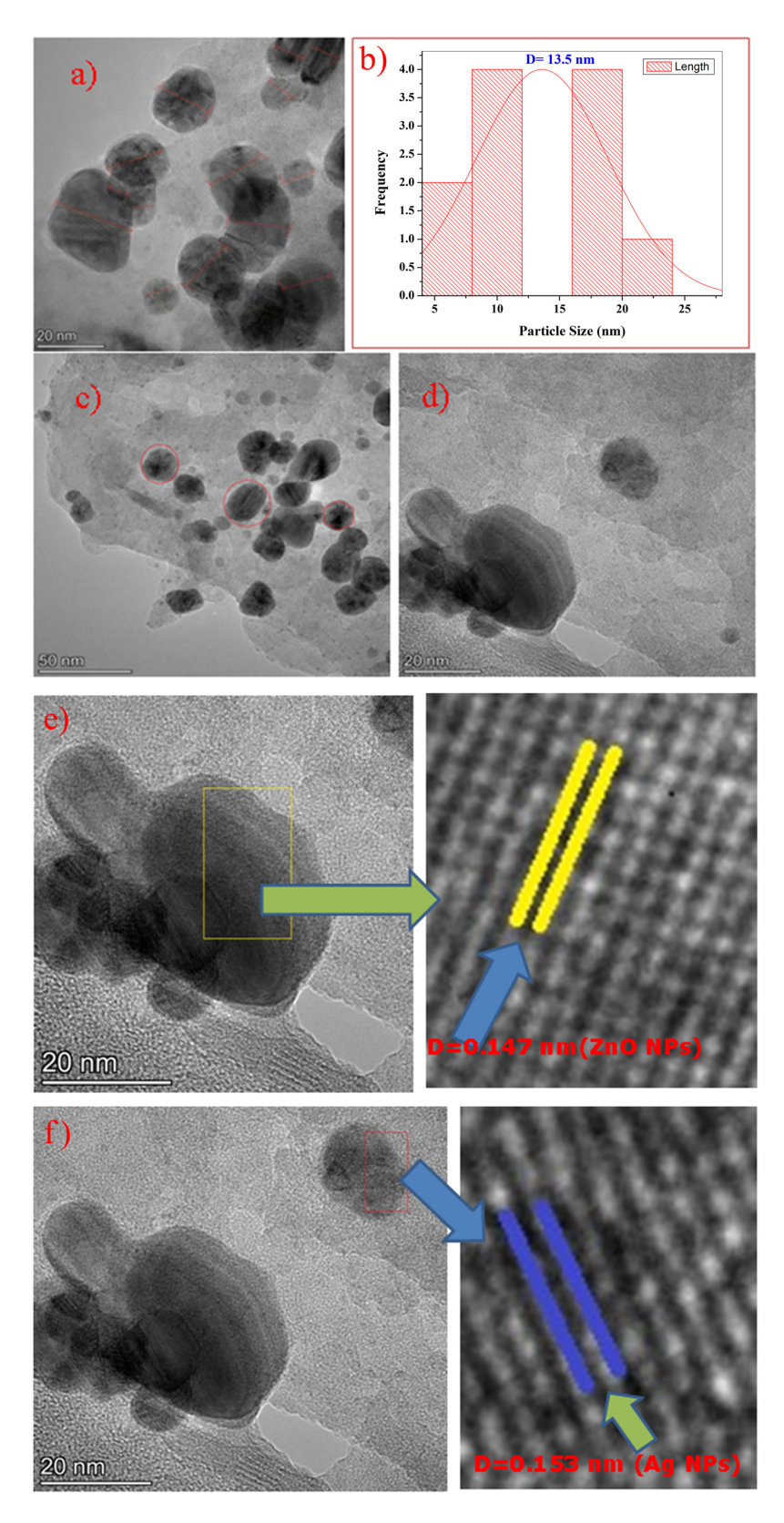
structure as mentioned above. The result also revealed that the effect was dose dependent. The strong antimicrobial action of Ag NPs is related to their nanoscale size and unique properties, changing the structure of cell membranes and even leading to cell death [10,66]. Their efficacy is not only to their nanoscale size but also to their reactivity toward bacteria DNA or amino acids. They can increase the permeability of cell membranes, produce reactive oxygen species, and interrupt replication of deoxyribonucleic acid by releasing silver ions [67], and as the concentration of these NPs increase the Ag ions released to the bacterial cell also increase. The present result also confirmed that the antibacterial activity of Ag NPs is dose dependent. This suggests that the inhibition zone is directly related to the concentration of Ag NPs.

The results of the antibacterial activity of ZnO are presented in Table 3. The results indicated that ZnO NPs showed an effective antibacterial activity against both tested strains, but its activities were less than that of Ag NPs. Generally, the results showed that the inhibitory effect of ZnO was found to have increased with the concentration (P < 0.05). A similar positive result was reported on the antibacterial properties of Ag NPs and ZnO NPs synthesized by biogenic methods [68].

In Table 3, zones of inhibition for standard Contrimoxazole (denoted with "Contr"), DMSO, and ZnO NPs (denoted with " X_4 ") against both Gram-negative (*E. coli*) and Gram-positive (*S. aureus*) are shown. Their inhibition zones were found to be 20.3 \pm 0.3, 6.1 \pm 0.1, and 10.3 \pm 0.3 mm at 20 mg·mL⁻¹, 10 \pm 0 at 10 mg·mL⁻¹, 7.6 \pm 0.3 mm at 5 mg·mL⁻¹, and 6.3 \pm 0.3 mm at 2.5 mg·mL⁻¹, respectively,

for Contrimoxazole, DMSO, and ZnO NPs (with different dosages) against E. coli ATCC 25922. However, inhibition zones were found to be 21.3 \pm 0.3, 6.1 \pm 0.2, and 11 \pm 0.6 mm at $20 \text{ mg} \cdot \text{mL}^{-1}$, 10.3 ± 0.3 at $10 \text{ mg} \cdot \text{mL}^{-1}$, $8 \pm 0 \text{ mm}$ at $5 \text{ mg} \cdot \text{mL}^{-1}$, and $7 \pm 0.6 \text{ mm}$ at $2.5 \text{ mg} \cdot \text{mL}^{-1}$, respectively, against S. aureus. A comparison of zone of inhibition values shows a larger value for Gram-positive bacteria (S. aureus) than that for Gram-negative (E. coli) bacterial strains toward standard and different dosages of ZnO NPs. The observed better inhibition zones show that the synthesized ZnO NPs disrupt the membrane with high rates of surface oxygen species generation and finally cause the death of pathogens [60]. ZnO shows good antibacterial property on both Grampositive and Gram-negative bacteria. But, the results were more pronounced against Gram-positive. The mechanisms include the release of antimicrobial ions [69], the interaction of NPs with microorganisms [70], and the formation of ROS by the effect of light radiation [71]. The release of antimicrobial ion/solubility of metal oxides is dependent on different factors such as the concentration of metal oxides, time of interaction, and the nature of microorganisms [69]. ZnO NPs cause disruption of bacterial membranes probably by the production of reactive oxygen species, such as superoxide and hydroxyl radicals. Moreover, ZnO NPs have positive zeta potential at their surface. This depends on the nature of the surface of different bacteria. Moreover, the antibacterial activity is reported to be dependent on the concentration of ZnO NPs and the impact of the type of surfactant used [59].

Composites of Ag/bentonite (denoted with " X_2 ") and ZnO/bentonite (denoted with " X_5 ") showed a good



 $\textbf{Figure 13:} \ \, \textbf{TEM images (a and c), NC histogram (b), HRTEM (d) of Ag/ZnO/bentonite NCs.} \ \, \textbf{(e) HRTEM images of Ag/ZnO/bentonite NCs.} \\ \ \, \textbf{(b) HRTEM images of Ag/ZnO/bentonite NCs.} \\ \ \, \textbf{(c) HRTEM images of Ag/ZnO/bentonite NCs.} \\ \ \, \textbf{(d) of Ag/ZnO/bentonite NCs.}$ (d = 0.147 nm ZnO NPs). (f) HRTEM images of Ag/ZnO/bentonite NCs (d = 0.153 nm Ag).

 $\begin{tabular}{ll} \textbf{Table 1:} d-Spacing values for ZnO NPs and Ag NPs from their SAED \\ pattern \end{tabular}$

NPs	1/2r (nm ⁻¹)	1/r (nm ⁻¹)	<i>r</i> (nm)	d-spacing(Å)	(hkl)
ZnO	8.096	4.048	0.247	2.47	(101)
	7.14	3.57	0.28	2.80	(100)
	7.72	3.86	0.259	2.59	(002)
	12.34	6.17	0.162	1.62	(110)
	10.52	5.26	0.190	1.90	(102)
	13.6	6.80	0.147	1.47	(103)
	13.62	6.81	0.37	1.37	(112)
	14.7	7.35	0.136	1.36	(201)
Ag	8.65	4.33	0.231	2.31	(111)
	9.52	4.76	0.210	2.10	(200)
	13.07	6.53	0.153	1.53	(220)
	16.66	8.33	0.120	1.20	(311)

antibacterial property. The inhibition zones of Ag/bentonite (denoted with " X_2 ") were found to be 14 \pm 0 mm at

 $10~{\rm mg\cdot mL^{-1}}$, $13.3~\pm~0.7$ at $5~{\rm mg\cdot mL^{-1}}$, $13~\pm~0.6~{\rm mm}$ at $2.5~{\rm mg\cdot mL^{-1}}$, and $12~\pm~0~{\rm mm}$ at $1.25~{\rm mg\cdot mL^{-1}}$ against E.~coli and $14.7~\pm~0~{\rm mm}$ at $10~{\rm mg\cdot mL^{-1}}$, $13.7~\pm~0.3$ at $5~{\rm mg\cdot mL^{-1}}$, $13.3~\pm~0.3~{\rm mm}$ at $2.5~{\rm mg\cdot mL^{-1}}$, and $12.3~\pm~0.3~{\rm mm}$ at $1.25~{\rm mg\cdot mL^{-1}}$ against S.~aureus. Similarly, ZnO/bentonite NCs (denoted with "X₅") show good antibacterial activities than ZnO NPs toward both tested bacterial strains (Table 2).

The results indicate that both the composites perform much better in inhibiting bacterial growth than Ag and ZnO NPs. The bactericidal effect of Ag and ZnO NPs in the composites can be attributed to their nano-scale properties. Both bulk materials of Ag and ZnO possess bactericidal properties. But at nano-scale, particles exhibit more pronounced bacterial effects toward a broad range of microorganisms. Their small size allows for better penetration and interaction with the bacteria, disrupting the cell membrane, when compared to their bulk material

Table 2: Zone of inhibition in mm for Ag NPs and Ag-based NCs at different concentrations

Types of NPs/NCs and bacterial strain		Mean of three replications and standard error $(\pm SE)$ of inhibition zones in mm for different concentrations						
S. No.	NPs/ NCs	Bacterial strain	10 mg⋅mL ⁻¹ (A)	5 mg⋅mL ⁻¹ (B)	2.5 mg·mL ⁻¹ (C)	1.25 mg⋅mL ⁻¹ (D)	Contrimoxazole (+ve)	DMSO (-ve)
1 X	X ₁	E. coli	11.6 ± 0.3	11.3 ± 0.3	11 ± 0.6	10.3 ± 0.3	20.3 ± 0.3	6 ± 0
		S. aureus	14.3 ± 0.3	13.3 ± 0.3	13 ± 0.3	11.3 ± 0.3	21.3 ± 0.3	6 ± 0
2	X_2	E. coli	14.3 ± 0.1	13.3 ± 0.3	13 ± 0.6	12.3 ± 0.0	20.2 ± 0.3	6 ± 0
		S. aureus	14.7 ± 0.3	13.7 ± 0.3	13.3 ± 0.3	12.3 ± 0.3	21.3 ± 0.3	6 ± 0
3	χ_3	E. coli	14.3 ± 0.3	13.7 ± 0.3	13.3 ± 0.3	12.3 ± 0.3	23.7 ± 0.3	6 ± 0
		S. aureus	17.3 ± 0.2	16.3 ± 0.3	15.3 ± 0.3	14.3 ± 0.3	24.3 ± 0.3	6 ± 0

Note: X₁, X₂, and X₃ are Ag NPs, Ag/bentonite NCs, and Ag/ZnO/bentonite NCs, respectively, E. coli ATCC 25922 and S. aureus ATCC 25923.

Table 3: Zone of inhibition in mm for synthesized ZnO NPs and ZnO-based NCs

Types of NPs/NCs and bacterial strain		Mean of three replications and standard error $(\pm SE)$ of inhibition zones in mm for different concentrations						
S. No.	NPs/ NCs	Bacterial strain	20 mg·mL ⁻¹ (A)	10 mg⋅mL ⁻¹ (B)	5 mg⋅mL ⁻¹ (C)	2.5 mg·mL ⁻¹ (D)	Contrimoxazole (25 µg) (+ve)	DMSO (-ve)
1	X ₄	E. coli	10.3 ± 0.3	10 ± 0	7.6 ± 0.3	6.3 ± 0.3	20.3 ± 0.3	6.1 ± 0.1
		S. aureus	11 ± 0.6	10.3 ± 0.3	8.1 ± 0.3	7 ± 0.6	21.3 ± 0.3	6.1 ± 0.2
2	X_5	E. coli	12.3 ± 0.3	10.6 ± 0.3	8.3 ± 0.3	6.6 ± 0.7	20.2 ± 0.3	6.1 ± 0.3
		S. aureus	12.3 ± 0.3	11.3 ± 0.3	8.6 ± 0.3	7 ± 0.6	22.3 ± 0.3	6.1 ± 0.2
3	X_6	E. coli	6.1 ± 0.3	6.1 ± 0.2	6.1 ± 0.2	6.1 ± 0.2	20.1 ± 0.2	6.1 ± 0.2
		S. aureus	6.1 ± 0.2	6.1 ± 0.2	6.1 ± 0.5	6.1 ± 0.3	22.1 ± 0.1	6.1 ± 0.1
4	X_7	E. coli	6.1 ± 0.3	6.1 ± 0.2	6.1 ± 0.1	6.1 ± 0.1	22.3 ± 0.3	6.1 ± 0.2
		S. aureus	6.1 ± 0.4	6.1 ± 0.2	6.1 ± 0.2	6.1 ± 0.2	22.7 ± 0.3	6.1 ± 0.2
5	X ₈	E. coli	9.1 ± 0.3	8.7 ± 0.3	8.3 ± 0.3	7.3 ± 0.3	22.7 ± 0.3	6.1 ± 0.2
	-	S. aureus	10 ± 0.0	9 ± 0.3	8.7 ± 0.3	8.3 ± 0.3	23.7 ± 0.3	6 ± 0.2

Note: X_4 , X_5 , X_6 , X_7 , and X_8 are ZnO NPs, ZnO/bentonite NCs, PB, Na-AB, and plant powder, respectively.

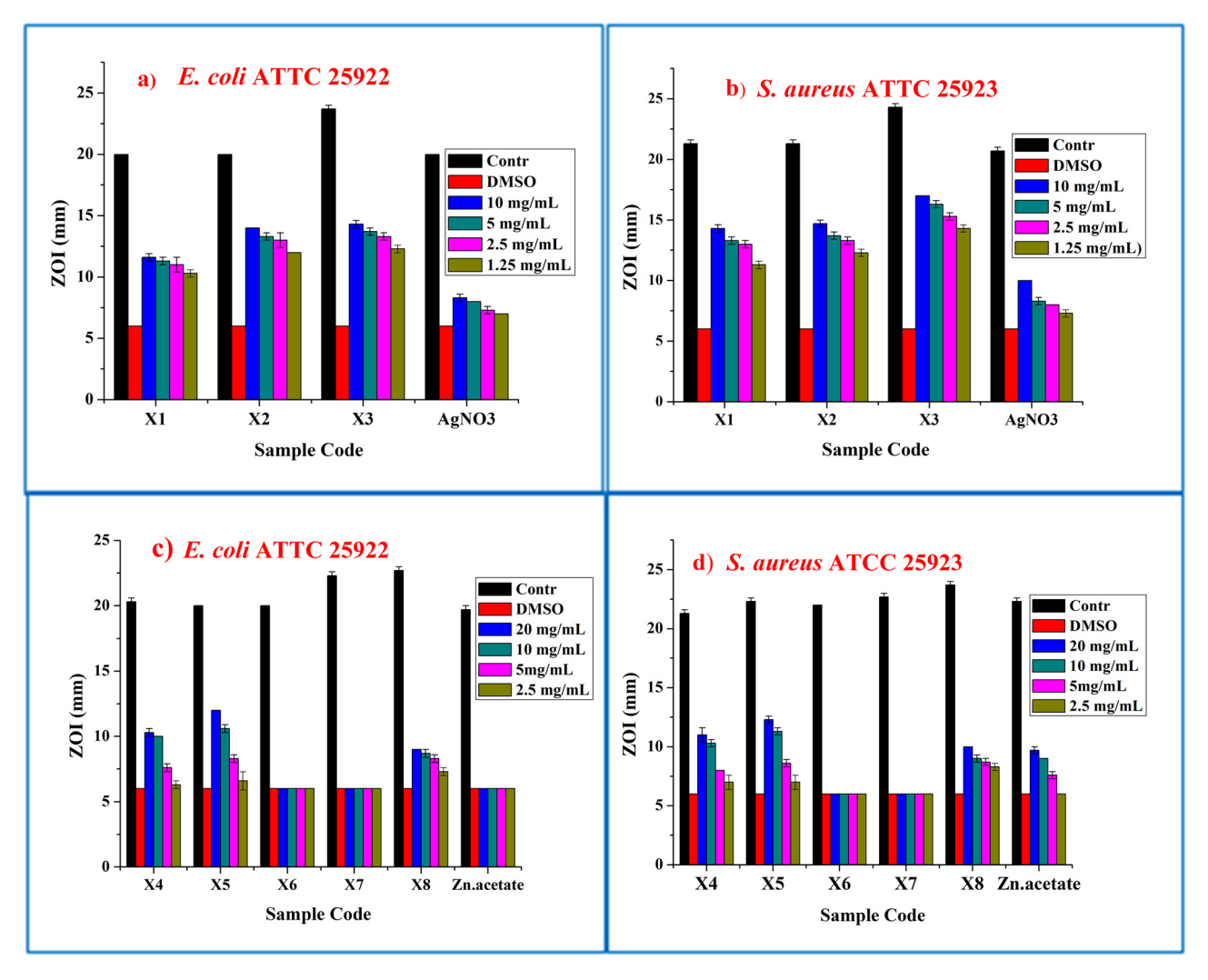


Figure 14: The display of the zone of inhibitions of the synthesized NPs (a and b) and NCs (c and d) at different concentrations against E. coli and S. aureus bacterial strains

Table 4: MIC ($\mu g \cdot mL^{-1}$) and MBC ($\mu g \cdot mL^{-1}$) of Ag/ZnO/bentonite NCs for E. coli and S. aureus bacterial strain

Bacterial strain	Strain no.	MIC (μg·mL ⁻¹)	$MBC~(\mu g{\cdot}mL^{-1})$
E. coli	ATCC 25922	156.25	312.5
S. aureus	ATCC 25923	78.125	156.25

[53]. Furthermore, a combination of the two composites (Ag/ZnO/bentonite, denoted "X₃") results in an excellent antibacterial activity. The antibacterial activity was more pronounced against the Gram-positive (S. aureus ATCC 25923) than the Gram-negative (E. coli) (Table 2). The inhibition zones of Ag/ZnO/bentonite NCs (denoted with "X₃") were determined to be 14.3 \pm 0.3 mm at 10 mg·mL⁻¹, $13.7 \pm 0.3 \,\mathrm{mm}$ at $5 \,\mathrm{mg \cdot mL}^{-1}$, $13.3 \pm 0.3 \,\mathrm{mm}$ at $2.5 \,\mathrm{mg \cdot mL}^{-1}$, and 12.3 \pm 0.3 mm at 1.25 mg·mL⁻¹ against E. coli and 17 \pm

0 mm at $10 \text{ mg} \cdot \text{mL}^{-1}$, $16.3 \pm 0.3 \text{ mm}$ at $5 \text{ mg} \cdot \text{mL}^{-1}$, $15.3 \pm$ $0.3 \,\mathrm{mm}$ at $2.5 \,\mathrm{mg \cdot mL^{-1}}$, and $14.3 \pm 0.3 \,\mathrm{mm}$ at $1.25 \,\mathrm{mg \cdot mL^{-1}}$ against S. aureus.

The results obtained suggest that the composite can be used as an effective antibacterial material. The enhanced antibacterial activity of the composites can be attributed to the chemical and physical properties of the NPs together with the large surface area of the Na-AB. This means that a large amount of NPs was highly dispersed per unit area of the bentonite surfaces, thus, maximizing antibacterial activity. In such combinations, NPs are largely attached on bentonite surface which ensure uniform dispersion, when compared with the bare NPs that tend to agglomerate and result with low performance or antibacterial properties.

There are a number of factors that could influence the results of the disc diffusion assay. First, the diameter of the zones is affected by the rate of diffusion of the antimicrobial compound and thus may not exactly represent the effectiveness of the sample's antimicrobial activity. Another important factor is the standardization of the inoculum size to 0.5McFarland turbidity. This inoculum size is important to ensure confluent or almost confluent lawn growth as a smaller inoculum size (such that single colonies are seen) may produce falsely large inhibition zones, while a bigger inoculum size (thick bacterial lawn) may produce falsely smaller zones instead [72].

To know the statistical significance of the data P-values were calculated for all the tests. The data presented in Figure 14 confirm the significance of the data obtained in the antibacterial study of the synthesized nanomaterials. As the obtained P-values were less than 0.05 (P < 0.05) in all the cases, it can be concluded that the data were statistically significant and acceptable.

3.2.2 MIC and MBC of Ag/ZnO/bentonite NCs

The results of the bactericidal effects of Ag/ZnO/bentonite NCs against selected bacterial strains via the MIC and the MBC are summarized in Table 4. The bactericidal effect of the NCs is dependent on the concentration of NCs and the initial bacterial concentration. In this study, the initial bacterial concentration was taken as 1×10^8 CFU·mL $^{-1}$. Ag/ZnO/bentonite NC showed a better antibacterial activity against both *S. aureus* and *E. coli*. The greater sensitivity of *S. aureus* toward this NC compared to *E. coli* is due to the presence of a thin peptidoglycan layer with an additional outer membrane consisting of lipopolysaccharide.

The MIC values of Ag/ZnO/bentonite NCs were found to be 156.25 and 78.125 $\mu g \cdot m L^{-1}$ for *S. aureus* and *E. coli*, respectively. The MBC values of Ag/ZnO/bentonite NCs were 312.5 and 156.25 $\mu g \cdot m L^{-1}$ for *S. aureus* and *E. coli*, respectively. These results observed that the *S. aureus* was most sensitive against Ag/ZnO/bentonite NCs.

4 Conclusions

The NCs, Ag/bentonite, ZnO/bentonite, and Ag/ZnO/bentonite were synthesized by a rapid and facile biogenic method using *H. abyssinica* plant leaf extract. The Na₂CO₃ activation of calcium-rich local bentonite resulted in the reduction of the interplanar space of the bentonite from 14 to 12.8 Å. The phytochemicals of *H. abyssinica* plant

leaf extract served as reducing and stabilizing agents toward the formation of NPs and NCs. Formation of all the NPs and NCs was confirmed by using XRD, FT-IR, SEM-EDX, and TEM techniques. The synergic effect of Ag NPs, ZnO NPs, and phyto-chemicals of *H. abyssinica* on the NC offered the superior antibacterial properties for Ag/ZnO/bentonite NCs.

Acknowledgments: The authors acknowledge Adama Science and Technology University for providing financial support for this project from the University 15th Cycle Research Grant and Adama Public Health Research and Referral Laboratory Center for providing laboratory facility for the antibacterial study.

Funding information: The financial support from the University 15th Cycle Research Grant and Adama Public Health Research, Adama Science and Technology University.

Author contributions: Conceptualization of the project idea, proposal writing for the grant, supervision of the project, and editing the manuscript: Enyew Amare Zereffa. Samples collection, experimental work, evaluation, analysis, and initial draft preparation: Adisu Girma. Reviewing and editing: Teshome Abdo. Characterization and reviewing: H. C. Ananda Murthy, C. R. Ravikumar, and Dhanalakshmi Muniswamy. Formal analysis and validation: Bayissa Bekele. All authors have accepted responsibility for the entire content of this manuscript and approved its submission.

Conflict of interest: The authors state no conflict of interest.

References

- [1] Farzana, R., S. M. Shamsuzzaman, and K. Z. Mamun. Isolation and molecular characterization of New Delhi metallo-betalactamase-1 producing superbug in Bangladesh. *Journal of Infection in Developing Countries*, Vol. 7, No. 3, 2013, pp. 161–168.
- [2] Xiao, X., Z. C. Wu, and K. C. Chou. A multi-label classifier for predicting the subcellular localization of gram-negative bacterial proteins with both single and multiple sites. *PLoS One*, Vol. 6, No. 6, 2011, pp. 1–10.
- [3] Hanczvikkel, A., A. Víg, and Á. Tóth. Survival capability of healthcare-associated, multidrug-resistant bacteria on untreated and on antimicrobial textiles. *Journal of Industrial Textiles*, Vol. 48, No. 7, 2018, pp. 1113–1135.
- [4] European Centre for Disease Prevention and Control. https:// www.ecdc.europa.eu/en/publications-data/antimicrobial-

- resistance-and-healthcare-associated-infections-annual# copy-toclipboard.
- [5] Alemayehu, T. Prevalence of multidrug-resistant bacteria in Ethiopia: a systematic review and meta-analysis. Journalof Global Antimicrobial Resistance, Vol. 26, 2021, pp. 133-139.
- de Souza Cândido, E., E. de Barros, M. H. Cardoso, and O. L. Franco. Bacterial cross-resistance to anti-infective compounds. Is it a real problem? Current Opinion in Pharmacology, Vol. 48, 2019, pp. 76-81.
- Ayukekbong, J. A., M. Ntemgwa, and A. N. Atabe. The threat of antimicrobial resistance in developing countries: causes and control strategies. Antimicrobial Resistance and Infection Control, Vol. 6, No. 1, 2017, pp. 1-8.
- Saravanakkumar, D., S. Sivaranjani, K. Kaviyarasu, A. Ayeshamariam, B. Ravikumar, S. Pandiarajan, et al. Synthesis and characterization of ZnO-CuO nanocomposites powder by modified perfume spray pyrolysis method and its antimicrobial investigation. Journal of Semiconductors, Vol. 39, No. 3, 2018, pp. 033001-033007.
- Stankic, S., S. Suman, F. Hagu, and J. Vidi. Pure and multi metal oxide nanoparticles: synthesis, antibacterial and cytotoxic properties. Journal of Nanobiotechnology, Vol. 14, No. 73, 2016, pp. 1-20.
- [10] Tahir, K., S. Nazir, A. Ahmad, B. Li, A. U. Khan, Z. U. H. Khan, et al. Facile and green synthesis of phytochemicals capped platinum nanoparticles and in vitro their superior antibacterial activity. Journal of Photochemistry & Photobiology, B: Biology, Vol. 166, 2017, pp. 246-251.
- [11] Gold, K., B. Slay, M. Knackstedt, and A. K. Gaharwar. Antimicrobial activity of metal and metal-oxide based nanoparticles. Advanced Therapeutics, Vol. 1, 2018, id. 1700033.
- [12] Dejen, K. D., E. A. Zereffa, H. C. A. Murthy, and A. Merga. Synthesis of ZnO and ZnO/PVA nanocomposite using aqueous Moringa oleifeira leaf extract template: antibacterial and electrochemical activities. Reviews on Advanced Materials Science, Vol. 59, 2020, pp. 464-476.
- [13] Franco, D., G. Calabrese, S. P. P. Guglielmino, and S. Conoci. Metal-based nanoparticles: antibacterial mechanisms and biomedical application. Microorganisms, Vol. 10, 2022, id. 1778.
- [14] Siddiqi, K. S., A. Husen, and R. A. K. Rao. A review on biosynthesis of silver nanoparticles and their biocidal properties. Journal of Nanobiotechnology, Vol. 16, 2018, pp. 1-28.
- [15] Khan, A. U., Q. Yuan, Z. U. H. Khan, A. Ahmad, F. U. Khan, K. Tahir, et al. An eco-benign synthesis of Ag NPs using aqueous extract of Longan fruit peel: antiproliferative response against human breast cancer cell line MCF-7, antioxidant and photocatalytic deprivation of methylene blue. Journal of Photochemistry & Photobiology, B: Biology, Vol. 183, 2018, pp. 67-373.
- [16] Yaqoob, A. A., K. Umar, and M. N. M. Ibrahim. Silver nanoparticles: various methods of synthesis, size affecting factors and their potential applications—a review. Applied Nanoscience, Vol. 10, 2020, pp. 1369-1378.
- [17] Bruna, T., F. Maldonado-Bravo, P. Jara, and N. Caro. Silver nanoparticles and their antibacterial applications. International Journal of Molecular Science, Vol. 22, No. 13, 2021, id. 720.
- [18] Akbar, A., M. Sadiq, A. Imran, N. Muhammad, Z. Rehman, N. Khan, et al. Synthesis and antimicrobial activity of zinc

- oxide nanoparticles against foodborne pathogens Salmonella typhimurium and Staphylococcus aureus. Biocatalysis and Agricultural Biotechnology, Vol. 17, 2019, pp. 36-42.
- [19] Abebe, B., E. A. Zereffa, A. Tadesse, and H. C. A. Murthy. Review on enhancing the antibacterial activity of ZnO: mechanisms and microscopic investigation. Nanoscale Research Letters, Vol. 15, No. 190, 2020, pp. 1-19.
- [20] Sergey, V. G., D. E. Burmistrov, D. A. Serov, M. B. Rebezov, A. A. Semenova, and A. B. Lisitsyn. A mini review of antibacterial properties of ZnO nanoparticles. Frontiers in Physics, Vol. 9, 2021, Article 641481. www.frontiersin.org.
- [21] Ishita, M., A. Sachdev, P. Dubey, S. U. Kumar, B. Bhushan, and P. Gopinat. Antibacterial activity and mechanism of Ag-ZnO nanocomposite on S. aureus and GFP-expressing antibiotic resistant E. coli. Colloids and Surfaces B: Biointerfaces, Vol. 115, No. 1, 2014, pp. 359-367.
- [22] Cuadra, J. G., L. Scalschi, B. Vicedo, M. Guc, V. I. Roca, S. Porcar, et al. ZnO/Ag nanocomposites with enhanced antimicrobial activity. Applied Sciences, Vol. 12, No. 10, 2022, id. 5023.
- [23] Hakimi, B., M. Ghorbanpour, and A. Feizi. ZnO/bentonite nanocomposites prepared with solid-state ion exchange as photocatalysts. Journal of Ultrafine Grained and Nanostructured Materials, Vol. 51, No. 2, 2018, pp. 139-146.
- Juang, R. S., S. H. Lin, and K. H. Tsao. Mechanism of the sorption of phenols from aqueous solutions onto surfactantmodified montmorillonite. Journal of Colloid and Interface Sciences, Vol. 254, 2002, pp. 234-241.
- [25] Murthy, H. C. A., T. D. Zeleke, C. R. Ravikumar, M. R. A. Kumar, and H. P. Nagaswarupa. Electrochemical properties of biogenic silver nanoparticles synthesized using Hagenia abyssinica (Brace) JF. Gmel. medicinal plant leaf extract. Journal of Materials Research Express, Vol. 7, No. 5, 2020, pp. 1-14.
- [26] Ahmad, A., Y. Wei, F. Syed, M. Imran, Z. U. H. Khan, K. Tahir, et al. Size dependent catalytic activities of green synthesized gold nanoparticles and electro-catalytic oxidation of catechol on gold nanoparticles modified electrode. RSC Advances, Vol. 5, 2015, id. 99364.
- [27] Tahira, K., S. Nazirb, B. Li, A. U. Khan, Z. U. H. Khan, P. Y. Gong, et al. Nerium oleander leaves extract mediated synthesis of gold nanoparticles and its antioxidant activity. Materials Letters, Vol. 156, 2015, pp. 198-201.
- [28] Gong, Z., L. Liao, G. Lv, and X. Wang. A simple method for physical purification of bentonite. Applied Clay Science, Vol. 119, 2016, pp. 294-300.
- [29] Magzoub, M. I., I. A. Hussein, M. S. Nasser, M. Mahmoud, A. S. Sultan, and A. Benamor. An investigation of the swelling kinetics of bentonite systems using particle size analysis. Journal of Dispersion Science and Technology, Vol. 41, No. 6, 2020, pp. 817-827.
- Shaikh, J. R. and M. Patil. Qualitative tests for preliminary phytochemical screening: an overview. International Journal of Chemical Studies, Vol. 8, No. 2, 2020, pp. 603-608.
- Golmohammadi, M., M. Honarmand, and S. Ghanbari. A green approach to synthesis of ZnO nanoparticles using jujube fruit extract and their application in photocatalytic degradation of organic dyes. Spectrochimica Acta Part A Molecular and Biomolecular Spectroscopy, Vol. 229, 2020, id. 117961.
- [32] Abdelkrim, S., A. Mokhtar, A. Djelad, F. Bennabi, A. Souna, A. Bengueddach, et al. Chitosan/Ag-bentonite

- nanocomposites: preparation, characterization, swelling and biological properties. *Journal of Inorganic and Organometallic Polymers and Materials*, Vol. 30, No. 3, 2020, pp. 831–840.
- [33] Hariram, M., V. Ganesan, S. Muthuramkumar, and S. Vivekanandhan. Functionalization of kaolin clay with silver nanoparticles by *Murraya koenigii* fruit extract-mediated bioreduction process for antimicrobial applications. *Journal of the Australian Ceramic Society*, Vol. 57, 2021, pp. 505–513.
- [34] Kassem, M. Performance evaluation of natural bentonite loaded with zinc oxide for the photocatalytic degradation of methyl red. *Romanian Journal of Chemistry*, Vol. 60, No. 10, 2015, pp. 957–963.
- [35] Krishnan, B. and S. Mahalingam. Ag/TiO₂/bentonite nano-composite for biological applications: synthesis, characterization, antibacterial and cytotoxic investigations. Advanced Powder Technology, Vol. 28, No. 9, 2017, pp. 2265–2280.
- [36] Asamoah, R. B., A. Yaya, P. Nbelayim, E. Annan, and B. Onwona-Agyeman. Development and characterization of claynanocomposites for water purification. *Materials(Basel)*, Vol. 13, No. 17, 2020, id. 3793.
- [37] Jamdagni, P., P. Khatri, and J. S. Rana. Green synthesis of zinc oxide nanoparticles using flower extract of *Nyctanthes arbortristis* and their antifungal activity. *Journal of King Saud University: Science*, Vol. 30, No. 2, 2018, pp. 168–175.
- [38] Shao, W., X. Liu, H. Min, G. Dong, Q. Feng, and S. Zuo. Preparation, characterization, and antibacterial activity of silver nanoparticle-decorated graphene oxide nanocomposite. *ACS Applied Materials Interfaces*, Vol. 7, No. 12, 2015, pp. 6966–6973.
- [39] Dadi, R., R. Azouani, M. Traore, C. Mielcarek, and A. Kanaev. Antibacterial activity of ZnO and CuO nanoparticles against gram positive and gram negative strains. *Materials Science* and Engeering C, Vol. 104, 2019, id. 109968.
- [40] Gupta, M. and A. Kumar. Comparison of minimum inhibitory concentration (MIC) value of statin drugs. A systematic review. Anti-Infective Agents, Vol. 17, No. 1, 2018, pp. 4–19.
- [41] Chikezie, I. O.. Determination of minimum inhibitory concentration (MIC) and minimum bactericidal concentration (MBC) using a novel dilution tube method. *African Journal of Microbiology Research*, Vol. 11, No. 23, 2017, pp. 977–980.
- [42] Ghamsari, M. S., S. Alamdari, W. Han, and H. H. Park. Impact of nanostructured thin ZnO film in ultraviolet protection. *International Journal of Nanomedicine*, Vol. 12, 2017, pp. 207–216.
- [43] Zhang, D., C. H. Zhou, C. X. Lin, D. S. Tong, and W. H. Yu. Synthesis of clay minerals. *Applied Clay Science.*, Vol. 50, 2010, pp. 1–11.
- [44] Colín-Luna, J. A., E. G. Zamora-Rodea, M. M. González-Brambila, E. Barrera-Calva, R. Rosas-Cedillo, A. K. Medina-Mendoza, et al. Biodiesel production using immobilized lipase supported on a zirconium-pillared clay. Effect of the immobilization method. *International Journal of Chemical Reactor* Engineering, Vol. 16, No. 1. 2018. id. 2017–0260.
- [45] Caglar, B., B. Afsin, A. Tabak, and E. Eren. Characterization of the cation-exchanged bentonites by XRPD, ATR, DTA/TG analyses and BET measurement. *Chemical Engineering Journal*, Vol. 149, No. 1–3, 2009, pp. 242–248.
- [46] El Miz, M., H. Akichoh, D. Berraaouan, S. Salhi, and A. Tahani. Chemical and physical characterization of moroccan bentonite

- taken from nador (north of Morocco). *American Journal of Chemistry*, Vol. 4, 2017, pp. 105-112.
- [47] Shah, L. A., N. S. Khattak, M. G. S. Valenzuela, A. Manan, and F. R. Valenzuela Díaz. Preparation and characterization of purified Na-activated bentonite from Karak (Pakistan) for pharmaceutical use. *Clay Minerals*, Vol. 48, No. 4, 2013, pp. 595–603.
- [48] Thi Lan Huong, V. and N. T. Nguyen. Green synthesis, characterization and antibacterial activity of silver nanoparticles using *Sapindus mukorossi* fruit pericarp extract. *Materials Today: Proceedings*, Vol. 42:, 2019, pp. 88–93.
- [49] Holzwarth, U., and N. Gibson. The Scherrer equation versus the "Debye-Scherrer equation". Nature Nanotechnology, Vol. 6, No. 9, 2011, id. 534.
- [50] Fakhari, S., M. Jamzad, and H. Kabiri Fard. Green synthesis of zinc oxide nanoparticles: a comparison. *Green Chemistry* Letters and Reviews, Vol. 12, No. 1, 2019, pp. 19–24.
- [51] Madhumitha, G., J. Fowsiya, N. Gupta, A. Kumar, and M. Singh. Green synthesis, characterization and antifungal and photocatalytic activity of *Pithecellobium dulce* peel-mediated ZnO nanoparticles. *Journal of Physics and Chemistry of Solids*, Vol. 127, 2019, pp. 43–51.
- [52] Chakraborty, T., A. Chakraborty, M. Shukla, and T. Chattopadhyay. ZnO-bentonite nanocomposite: an efficient catalyst for discharge of dyes, phenol and Cr(VI) from water. *Journal of Coordination Chemistry*, Vol. 72, No. 1, 2019, pp. 53-68.
- [53] Motshekga, S. C., S. S. Ray, M. S. Onyango, and M. N. B. Momba. Microwave-assisted synthesis, characterization and antibacterial activity of Ag/ZnO nanoparticles supported bentonite clay. *Journal of Hazardous Materials*, Vol. 262, 2013, pp. 439–446.
- [54] Dupraz, M., G. Beutier, D. Rodney, D. Mordehai, and M. Verdier. Signature of dislocations and stacking faults of face-centred cubic nanocrystals in coherent X-ray diffraction patterns: a numerical study. *Journal of Applied Crystallography*, Vol. 48, 2015, pp. 621–644.
- [55] Hashim, F. S., A. F. Alkaim, S. M. Mahdi, and A. H. Omran Alkhayatt. Photocatalytic degradation of GRL dye from aqueous solutions in the presence of ZnO/Fe₂O₃ nanocomposites. *Composites Communications*, Vol. 16, 2019, pp. 111–116.
- [56] Krishnan, B. and S. Mahalingam. Improved surface morphology of silver/copper oxide/bentonite nanocomposite using aliphatic ammonium based ionic liquid for enhanced biological activities. *Journal of Molecular Liquids*, Vol. 241, 2017b, pp. 1044–1058.
- [57] Kumar, S., M. M. Abedin, A. K. Singh, and S. Das. Role of phenolic compounds in plant-defensive mechanisms. *Plant Phenolics in Sustainable Agriculture*, Vol. 20, 2020, pp. 517–532.
- [58] Awwad, A. M., B. Albiss, and A. L. Ahmad. Green synthesis, characterization and optical properties of zinc oxide nanosheets using *Olea europea* leaf extract. *Advanced Materials Letters*, Vol. 5, No. 9, 2014, pp. 520–524.
- [59] Dobrucka, R. and J. Długaszewska. Biosynthesis and antibacterial activity of ZnO nanoparticles using *Trifolium pratense* flower extract. *Saudi Journal of Biological Science*, Vol. 23, No. 4, 2016, pp. 517–523.
- [60] Suresh, J., G. Pradheesh, V. Alexramani, M. Sundrarajan, and S. I. Hong. Green synthesis and characterization of zinc oxide

- nanoparticle using insulin plant (*Costus pictus* D. Don) and investigation of its antimicrobial as well as anticancer activities. *Advances in Natural Sciences: Nanoscience and Nanotechnology*, Vol. 9, No. 1, 2018, pp. 1–9.
- [61] Yuvakkumar, R., J. Suresh, B. Saravanakumar, A. Joseph Nathanael, S. I. Hong, and V. Rajendran. Rambutan peels promoted biomimetic synthesis of bioinspired zinc oxide nanochains for biomedical applications. Spectrochimica Acta Part A: Molecular and Biomolecular Spectroscopy, Vol. 137, 2015, pp. 250–258.
- [62] Rajendran, S. P. and K. Sengodan. Synthesis and characterization of zinc oxide and iron oxide nanoparticles using Sesbania grandiflora leaf extract as reducing agent. Journal of Nanoscience, Vol. 2017, 2017, id. 7.
- [63] Minatel, I. O., C. V. Borges, H. Alonzo, G. Hector, G. Gomez, et al. Phenolic compounds: functional properties, impact of processing and bioavailability. *Phenolic Compounds Biological Activity*. Open. Science., 2017, pp. 1–24.
- [64] Gonelimali, F. D., J. Lin, W. Miao, J. Xuan, F. Charles, M. Chen, et al. Antimicrobial properties and mechanism of action of some plant extracts against food pathogens and spoilage microorganisms. Front Microbiology, Vol. 9, 2018, pp. 1–9.
- [65] Slavin, Y. N., J. Asnis, U. O. Häfeli, and H. Bach. Metal nanoparticles: understanding the mechanisms behind antibacterial activity. *Journal of Nanobiotechnology*, Vol. 15, No. 1, 2017, pp. 1–20.
- [66] Kukushkina, E. A., S. I. Hossain, M. C. Sportelli, N. Ditaranto, R. A. Picca, and N. Cioffi. Ag-based synergistic antimicrobial

- composites. A critical review. *Nanomaterials*, Vol. 11, No. 7, 2021, pp. 1–36.
- [67] Yin, I. X., J. Zhang, I. S. Zhao, M. L. Mei, Q. Li, and C. H. Chu. The antibacterial mechanism of silver nanoparticles and its application in dentistry. *International Journal Nanomedicine.*, Vol. 15, 2020, pp. 2555–2562.
- [68] Mehran, A., M. R. Hamblin, and J. F. Kennedy. Antimicrobial applications of lichens: secondary metabolites and green synthesis of silver nanoparticles: a review. *Nano Micro Biosystems.*, Vol. 1, No. 1, 2022, pp. 15–21.
- [69] Espitia, P. J. P., N. de F. F. Soares, J. S. dos R. Coimbra, N. J. de Andrade, R. S. Cruz, and E. A. A. Medeiros. Zinc oxide nanoparticles: synthesis, antimicrobial activity and food packaging applications. *Food and Bioprocess Technology*, Vol. 5, No. 5, 2012, pp. 1447–1464.
- [70] Lin, H., M. Yang, H. Tang, and F. Pan. Effect of minor Sc on the microstructure and mechanical properties of AZ91 magnesium alloy. *Progress in Natural Science: Materials International*, Vol. 28, No. 1, 2018, pp. 66–73.
- [71] Jalal, R., E. K. Goharshadi, M. Abareshi, M. Moosavi, A. Yousefi, and P. Nancarrow. ZnO nanofluids: green synthesis, characterization, and antibacterial activity. *Materials Chemistry and Physics*, Vol. 121, No. 1–2, 2010, pp. 198–201.
- [72] Razmavar, S., M. A. Abdulla, S. B. Ismail, and P. Hassandarvish. Antibacterial activity of leaf extracts of Baeckea frutescens against methicillin-resistant Staphylococcus aureus. Biomed Research International, Vol. 2014, 2014, pp. 1–5, id. 521287.